Title
On the development of rod-based models for pneumatically actuated soft robot arms: A five-parameter constitutive relation

Authors
de Payrebrune, Kristin M
O'Reilly, Oliver M

Publication Date
2017-08-01

DOI
10.1016/j.ijsolstr.2017.05.003

On the Development of Rod-Based Models for Pneumatically Actuated Soft Robot Arms: A Five-Parameter Constitutive Relation

Kristin M. de Payrebrune[a], Oliver M. O'Reilly[a]

[a]*Department of Mechanical Engineering, University of California at Berkeley, Berkeley CA 94720, USA*

Abstract

While soft robots have many attractive features compared to their hard counterparts, developing tractable models for these highly deformable, nonlinear, systems is challenging. In a recent paper, the authors published a non-classic, five-parameter constitutive relation for a rod-based model of a widely used, pneumatically actuated soft robot arm. It is natural to ask if the complexity of the relation can be eliminated by redesigning the actuator? To this end, finite element models and experimental results are used to further explore the five-parameter constitutive relation. For multiple designs of the pneumatically actuated soft robot arm, we are able to demonstrate how finite element models can be employed in place of experiments to specify the constitutive relations and how the relations are scalable by actuator length and applied pressure. Our primary result is the finding that the five-parameter constitutive relation is germane to pneumatically actuated soft robot arms and the parameters for this relation can be determined by three finite element simulations.

*Corresponding author, Tel.: +1 510 642 0877,oreilly@berkeley.edu

Keywords: Soft robots, Rod theories, Finite element model, Pneu-net actuator, Constitutive relations, Elastica

1. Introduction

As a novel field of robotics, the enormous potential of soft actuators to assist mobility, handle fragile objects, and enable new design strategies has resulted in a surge of design, fabrication, and research activities. Ambulating soft robots (Shepherd et al. (2011); Tolley et al. (2014); Yang et al. (2015)), swimming soft robots (Marchese et al. (2014); Suzumori et al. (2007)), as well as elephant trunk-like actuators (Calisti et al. (2011); Martinez et al. (2013)), gripping devices (Stokes et al. (2014); Suzumori (1996)), and biomedical devices for rehabilitation (Polygerinos et al. (2013)) are among the many research topics considered in this area in the past two decades. While the theoretical framework for modeling soft robots is based on well-known concepts in continuum mechanics, developing tractable, yet faithful, models is challenging (Kim et al. (2013); Pfeifer et al. (2012); Majidi (2013)). For soft robots with long, slender geometries, nonlinear, rod-based models have been examined to explore the dynamics of these actuators (cf., e.g., Webster and Jones (2010); Gravagne et al. (2003); Plaut (2015); Renda et al. (2012); Zhou et al. (2015); Santillan et al. (2006)). By way of contrast, design studies examining the influence of the geometry on performance have primarily featured models based on the finite element method (cf., e.g., Suzumori et al. (2007); Polygerinos et al. (2013); Suzumori et al. (1997)). We also note that complementary quantitative measurements of the deformation of soft robot actuators are now starting to appear (cf., e.g., Majidi et al. (2013); de Payrebrune and O'Reilly (2016b)).

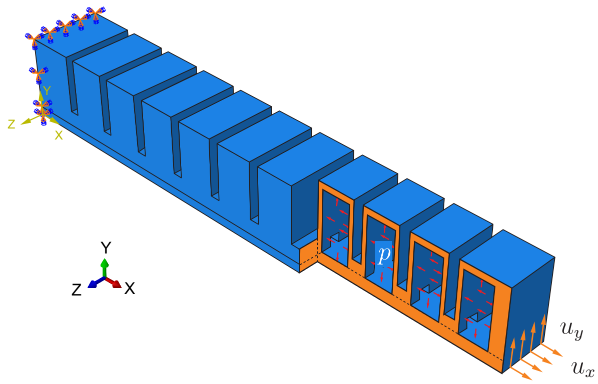

Figure 1: *Finite element model of the pneu-net soft actuator with fixed boundary condition, pressurized cavities and defined end-deformations.*

Of particular interest to the authors is the development of rod-based models for soft robot actuators. As a first example, we considered the popular pneu-net actuator that features in the work of George Whitesides and his research group (Shepherd et al. (2011); Ilievski et al. (2011)). For a given actuator, such as the one shown in Figure 1, we measured the intrinsic curvature κ_0 induced by a change in pressure, and then, for a given pressure and terminal load, measured the moment-curvature relations. We expected the classical result that the internal moment would be linearly proportional to a constant flexural rigidity and the difference in the curvature and intrinsic curvature: $\kappa - \kappa_0$. However, as discussed in de Payrebrune and O'Reilly (2016b), the relations we found for the flexural rigidity were far more complex and required five parameters to approximate. It is natural to ask if such a constitutive relation is only applicable to the pneu-net actuator or if it is germane to all pneumatic actuators? A related issue is the possibility of designing an actuator that has a simple constitutive relation with a minimum number of parameters. In the present paper, we use finite element models and experiments to explore a broad range of designs in the hopes of finding actuators with the simplest possible constitutive relations. However, we find that the five-parameter constitutive relation is germane to the wide range of actuator designs we consider. In addition, we note that the parameters for this relation can be determined by three finite element simulations.

In the sequel, we outline the parameterization routine and give detailed information on the finite element simulations and the rod model in Section 2. Then, using the example of a well-known soft pneu-net actuator, we show how the constitutive relations are computed in Section 3 and validate the finite element-based results using experiments. We then explore modified geometries and designs in Section 4. Our conclusions and a summary of our main results are presented in Section 5.

2. Material and Methods

In order to use a model based on rod theory to describe the mechanics of a deformable soft robot actuator, various parameters in the model need to be prescribed. Among the parameters required for the rod-based model are those relating the bending moment to a change in curvature. The prescriptions are obtained using a series of comparisons with experiments and finite element models. In this section of the paper, the prescription of the parameters and the benchmarking experiments are discussed.

2.1. Elastic Rod Model

Development of a rod-based model for the soft actuator starts by identifying the centerline of the rod with a material curve on the soft actuator. In

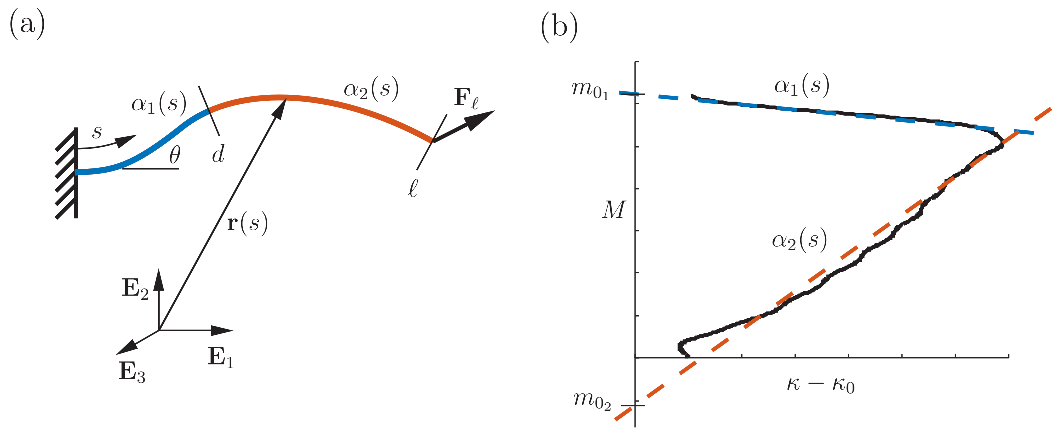

Figure 2: *(a) Rod model of the pneu-net soft actuator where one end is clamped and the other end is subject to a terminal load* $\mathbf{F}_\ell$*. (b) Illustration of the non-classical and position dependent constitutive relation, obtained from finite element simulations, for the bending moment* M *that was discussed in de Payrebrune and O'Reilly (2016b). The parameters* α_1 *and* α_2 *are discussed in Section 3 of the present paper.*

this endeavor, we assume that the actuator lies in the horizontal plane and we closely follow our earlier works Zhou et al. (2015); de Payrebrune and O'Reilly (2016b), and Majidi et al. (2012). We assume the material curve is inextensible and of length ℓ. Referring to Figure 2(a), a material point on the centerline of the rod can be identified by the arc-length coordinate $s \in [0, \ell]$ and its position vector $\mathbf{r}$ relative to a fixed origin has the representation

$$\mathbf{r}\,(s) = x\,(s)\,\mathbf{E}_1 + y\,(s)\,\mathbf{E}_2. \tag{1}$$

To characterize the bending of the rod, we define an angle $\theta = \theta(s)$, which is subtended by the unit tangent vector to the centerline of the rod with the horizontal: $\frac{\partial \mathbf{r}}{\partial s} = \cos(\theta(s))\mathbf{E}_1 + \sin(\theta(s))\mathbf{E}_2$. We also note the integral relations between the Cartesian coordinates $x = x(s)$ and $y = y(s)$ and the angle $\theta = \theta(s)$:

$$x\left(s = s_i\right) = x(s = 0) + \int_0^{s_i} \cos(\theta(\xi))\, \mathrm{d}\xi,$$
$$y\left(s = s_i\right) = y(s = 0) + \int_0^{s_i} \sin(\theta(\xi))\, \mathrm{d}\xi. \tag{2}$$

To model the experiments of interest, the end $s = 0$ of the rod is clamped, and the pressure-induced deformation of the actuator is modeled by a pressure-dependent intrinsic curvature field: $\kappa_0 = \kappa_0(s, p)$. We also allow situations where the other end $(s = \ell)$ of the rod is subject to a terminal load $\mathbf{F}_\ell$, as illustrated in Figure 2, which results in the force-induced curvature field $\kappa(s, p)$ of the current state.

The deformed shape of the rod can be found from the balance laws of the static case for linear and angular momentum:

$$\frac{\partial \mathbf{n}}{\partial s} = \mathbf{0},$$
$$\frac{\partial}{\partial s}\left(\mathbf{M} + \mathbf{r} \times \mathbf{n}\right) = \mathbf{0}. \tag{3}$$

Here, $\mathbf{n} = \mathbf{n}(s)$ is the contact force in the rod, $\mathbf{M} = M(s)\mathbf{E}_3$ is the bending moment in the rod, and we have assumed that no body forces or tractions on the lateral surface of the rod are present. We assume that the bending moment $M = M(s)$ is linearly dependent on the difference between the curvature κ of the current state and intrinsic curvature κ_0 of the reference state:

$$M = D(s)\left(\kappa - \kappa_0\right) + M_0. \tag{4}$$

Here, $D(s)$ is a position-dependent flexural rigidity and M_0 is a constant. In our work de Payrebrune and O'Reilly (2016b) on the pneu-net actuator, we found that the constitutive parameters D and M_0 were piecewise constants (cf. Figure 2(b)). As a result, five parameters were needed to prescribe (4), for which we introduced $s = d$, the position of discontinuity in $D(s)$. In addition, it is important to note that the intrinsic curvature κ_0 is not only dependent on the pressure p, but also varies along the length of the rod: $\kappa_0 = \kappa_0(s, p)$.

For a rod subject to a terminal load $\mathbf{F}_\ell$ at $s = \ell$, we can use $(3)_1$ to find that $\mathbf{n}(s) = \mathbf{F}_\ell$: that is, $\mathbf{n}(s)$ is constant throughout the rod. Noting that the bending moment vanishes at $s = \ell$, we can then use $(3)_2$ to show that $\mathbf{M}(s)$ can be determined from a measurement of $\mathbf{r}(s)$ and the terminal loading:

$$\mathbf{M}(s) = \underbrace{\mathbf{M}(\ell)}_{=0} + (\mathbf{r}(\ell) - \mathbf{r}(s)) \times \mathbf{F}_\ell. \tag{5}$$

This identity is independent of the constitutive relation for the elastic rod and we exploit this independence in the sequel by using (5) to determine the constitutive relation for the rod.

2.2. Finite Element Model

We developed a finite element model of the soft robot actuator using a standard explicit model in Abaqus\CAE 6.14. (Dassault Systems). The model is similar to the one described in Holland et al. (2014) and the associated online resource Soft Robotics Toolkit (2017). After the geometry of the soft actuator was loaded and assembled, we then defined the boundary conditions and introduced air pressure into the cavities (cf. Figure 1).

In addition to the simulation of a purely pressurized actuator with free boundaries (Test I), two simulations were performed and compared to the experiments from de Payrebrune and O'Reilly (2016b):

Test I: The soft robot is deformed by changing the pneumatic pressure in the free-free arm. In combination with Test II, this test is designed to analyze the dependence of the intrinsic curvature profile $\kappa_0\,(s, p)$ on the boundary conditions (cf. Figure 3(a)).

Test II: One end of the actuator is clamped, the other end is free, and the soft robot is then deformed by changing the pneumatic pressure in the arm. This test of the cantilevered actuator is designed to measure the intrinsic curvature profile $\kappa_0\,(s, p)$ (cf. Figure 3(b)).

Test III: One end of the actuator is clamped, and on the other end either a force $\mathbf{F}_\ell$ is applied (for experiments), or the displacement is defined (finite element simulation). The soft robot is then deformed by changing the pneumatic pressure in the arm. This test is designed to measure the curvature profile $\kappa(s, p)$ and the bending moment $M(s)$ (cf. Figure 3(c)).

To facilitate comparisons with experiments, the reaction force at the end point in the finite element models is recorded for Test III.

A variety of constitutive relations for the finite element model are possible. To examine the optimal selection, we performed monotonic and cyclic tensile tests according to ISO 37 on dumb-bell samples of Elastosil M4601 silicone rubber at our partner's facility, the Institute for Machine Elements, Design and Manufacturing (IMKF) at the Technische Universität Bergakademie Freiberg (Germany). Figure 4 illustrates a typical measurement of a monotonic tensile test with a change in the stiffness for higher stretches exceeding 150 %. With a least-square approximation, we computed the Young's moduli

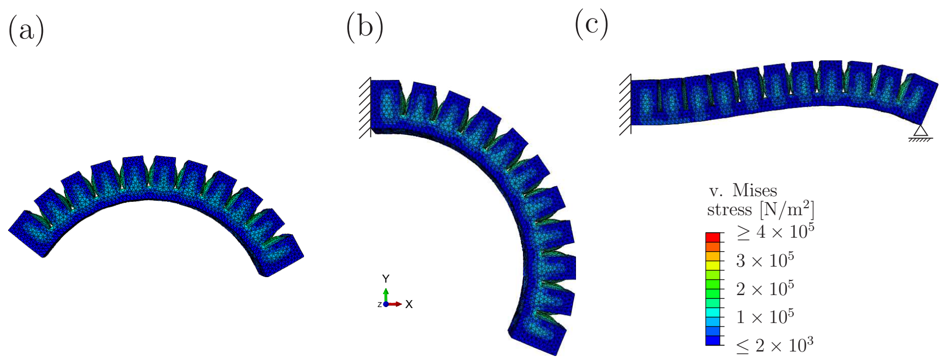

Figure 3: *Illustration of the deformation of the initially pressurized actuator which is unrestrained (Test I) in (a), clamped at one end (Test II) in (b) and clamped at one end and constrained in the vertical direction at the other end (Test III) in (c) for a pressurization of* 37 *kPa.*

$E_L = 6.5 \times 10^5$ N/m^2 and $E_H = 1.2 \times 10^6$ N/m^2 and assumed a Poisson ratio of $\nu = 0.495$ for the rubber material.

After evaluating other constitutive models, such as the Neo-Hookean, Mooney-Rivlin, and Yeoh models, using cyclic tensile tests, we concluded that the best constitutive relation for the applications in this paper was a St. Venant-Kirchhoff constitutive relation for the silicone rubber where $E = E_H$ and $\nu = 0.495$.

To validate the selected St. Venant-Kirchhoff model, we calculated the deformation of the soft actuator design provided in Holland et al. (2014)[1], and compared the pressure-dependent deformation with experiments (cf. Figure 5). The experiments and concomitant protocols were identical to those discussed in de Payrebrune and O'Reilly (2016b). During experiments, the actuator was aligned horizontally on a smooth surface in order to reduce

[1]See, in addition, the online resource Soft Robotics Toolkit (2017).

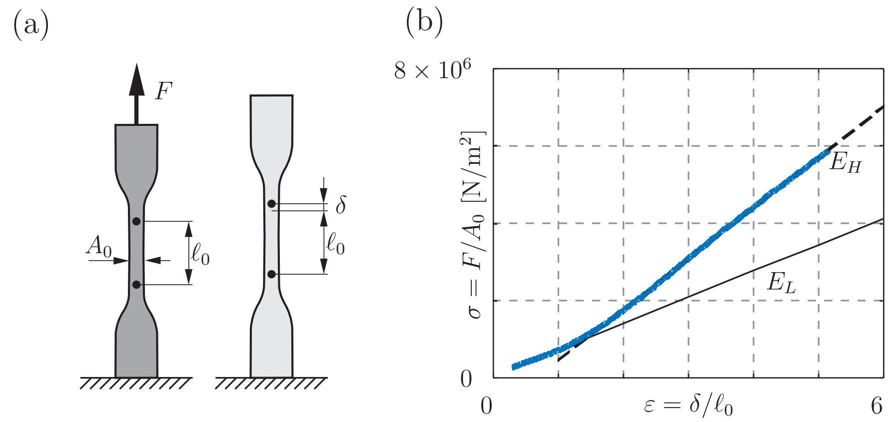

Figure 4: *Measurement of the stress-strain relation of Elastosil M4601 silicone rubber obtained from a quasi-static tensile test with a deformation rate of* 200*mm/s. The Young's moduli for low strain* $E_L(\varepsilon < 1.5)$ *and large strain* $E_H(\varepsilon > 1.5)$ *are indicated by the black lines.*

gravitational effects, and, so, we ignored gravity in our finite element simulations. Further, for Test III, a force was applied at the end of the actuator using strings and the two components of the force were measured by spring dynamometers. In the finite element simulation, the end-position of the actuator was defined according to the measurements and the resulting reaction forces were compared with the experimental measurements. Figure 6 illustrates the deformation of the soft actuator for different pressures. We found very good agreement between the finite element simulation and the experiment for both Tests II and III.

3. Prescriptions for the Parameters for the Rod Model

The parameters needed for the rod model include its overall length ℓ, mass m, and a constitutive relation that relates the bending moment M to the change in curvature $\kappa - \kappa_0$. In addition, a relation between the air pressure

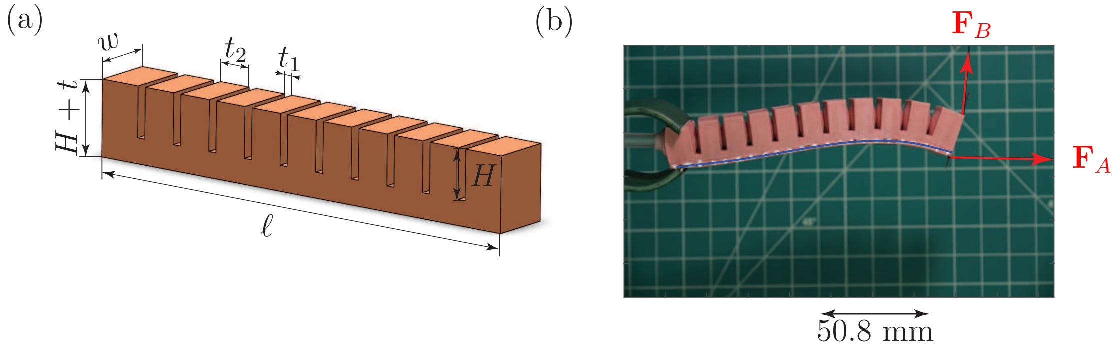

Figure 5: *The pneumatically actuated soft robot limb. (a) Schematic of the actuator with the labeling of its dimensions; and (b) the actuator which is clamped at one end and loaded with a force* $\mathbf{F}_A + \mathbf{F}_B = 0.175\mathbf{E}_1 + 0.07\mathbf{E}_2$ *at the other end while subject to an air pressure of* 31 *kPa. The dimensions of the arm featured in (a) and (b) and throughout this paper are* $w = 15$ *mm,* $H = 12$ *mm,* $t = 3$ *mm ,* $t_1 = 2$ *mm,* $t_2 = 8$ *mm, and* $\ell = 112$ *mm. The experimental set up is identical to that used in de Payrebrune and O'Reilly (2016b).*

p and the intrinsic curvature profile $\kappa_0(s)$ is required. In this section of the paper, a series of three tests on the actuator are described. These tests help to determine the aforementioned parameters and curvature profile, and are identical to those described in de Payrebrune and O'Reilly (2016b). Several details from this paper are recalled here. In contrast to the comparisons performed in our earlier work, here the experiments are compared to a finite element model of the actuator. The finite element model will enable us to make conclusions for a wide variety of designs in the later sections of this paper.

The first pair of tests, Test I and Test II, is designed to determine $\kappa_0(s)$ as a function of p. To this end, a material curve $\mathcal{A}$ of length ℓ is identified that runs the length of the actuator, and the corresponding curve is identified

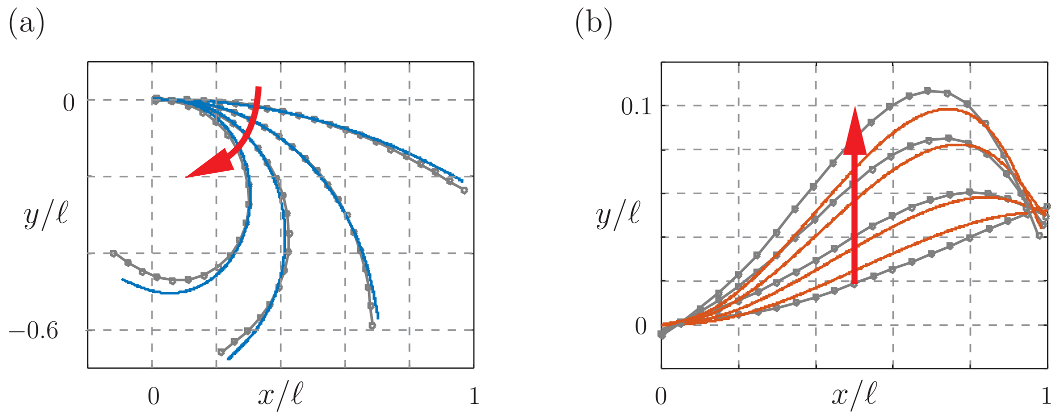

Figure 6: *Measured and simulated (using a finite-element model) displacements of a material line of (a) a pressurized cantilevered actuator (Test II) and (b) of a terminally loaded actuator (Test III). The pressure p in this figure takes the values 5, 17, 31 and 45 kPa and the arrows indicate increasing values of p. The dotted lines correspond to the experimental data.*

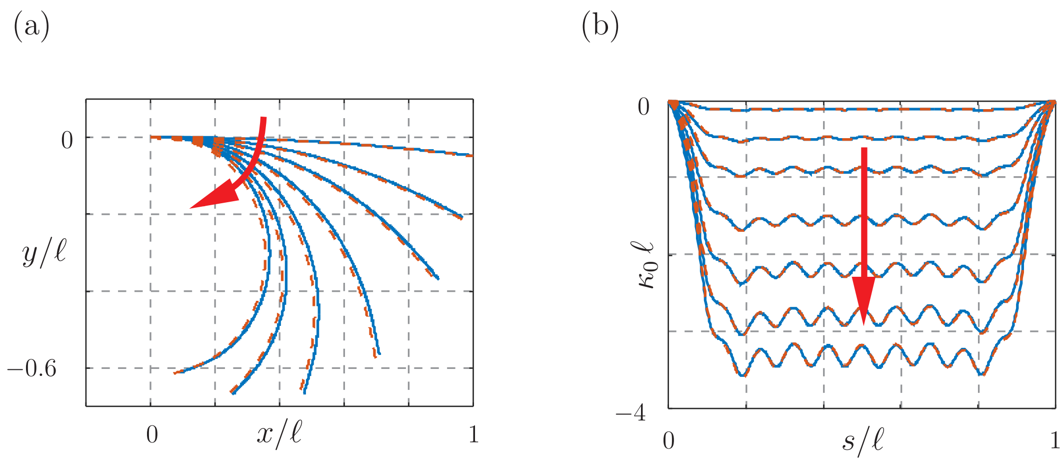

Figure 7: *(a) Calculated displacements using the finite element model and (b) computed intrinsic curvature of a material line of a pressurized cantilevered actuator. The results where the actuator is not clamped (Test I) are drawn as solid blue lines and those for the case where the actuator is clamped at one end (Test II) are drawn as a dashed red line. The pressure p in this figure takes the values 1, 5, 10, 17, 24, 31 and 37 kPa and the arrows indicate increasing values of p.*

in the companion finite element model. If we denote the position vector of a point on this curve by $\mathbf{R}(s)$, then by measuring $X(s) = \mathbf{R}(s) \cdot \mathbf{E}_1$ and $Y(s) = \mathbf{R}(s) \cdot \mathbf{E}_2$, the curvature κ_E of the curve can be found using the identity

$$\kappa_E(s) = \frac{X'Y'' - X''Y'}{\left(X'^2 + Y'^2\right)^{3/2}}, \tag{6}$$

where the prime denotes the partial derivative with respect to s and the subscript E denotes experimental data. To eliminate effects of local deformation of the cavities in the finite element model, or, of irregularities of optically measured marker positions in the case of measurements, we smooth the nodal values by performing a Gaussian process regression (cf. Aissiou et al. (2013)). We use (6) in conjunction with Test II to determine the intrinsic curvature profile $\kappa_0\,(s,p)$ by identifying $\kappa_E = \kappa_0$ for a given pressure and location s along the material curve.

To verify that the curvature profile $\kappa_0\,(s,p)$ is not related to the boundary conditions, we compared the deformation and the intrinsic curvature produced in Tests I and II (cf. Figure 7). After some initial alignment, we found that the deformations for a given pressure coincided in both cases. That is, the function $\kappa_0\,(s,p)$ was not affected by the clamping conditions present in Test II. This independence justifies our use of experiments featuring a clamped actuator to determine the intrinsic curvature profile. A representative sample of experimental results along with a comparison to a finite element model is shown in Figure 8.

To determine the parameters for the constitutive relation (4) for the bending moment, we turn to Test III. For a given pressure, we assume that $\kappa_0(s,p)$ is determined when $\mathbf{F}_\ell = \mathbf{0}$ in Test II. Then, in Test III, for a given $\mathbf{F}_\ell$, the position vector $\mathbf{R}$ of the material curve $\mathcal{A}$ on the actuator is recorded. The moment $\mathbf{M}(s)$ is determined using an identity and an identification:

$$\mathbf{M}(s) = (\mathbf{r}(\ell) - \mathbf{r}(s)) \times \mathbf{F}_\ell, \qquad \mathbf{r}(s) = \mathbf{R}(s), \tag{7}$$

where $\mathbf{M}(\ell) = 0$. The curvature κ can be determined using the identity (6). For the finite element model, the moment can also be calculated by a weighted integration of the traction vector through a cross-section. However, we found that such a procedure gave noisy data, especially when the actuator contains cells of isolated air chambers.

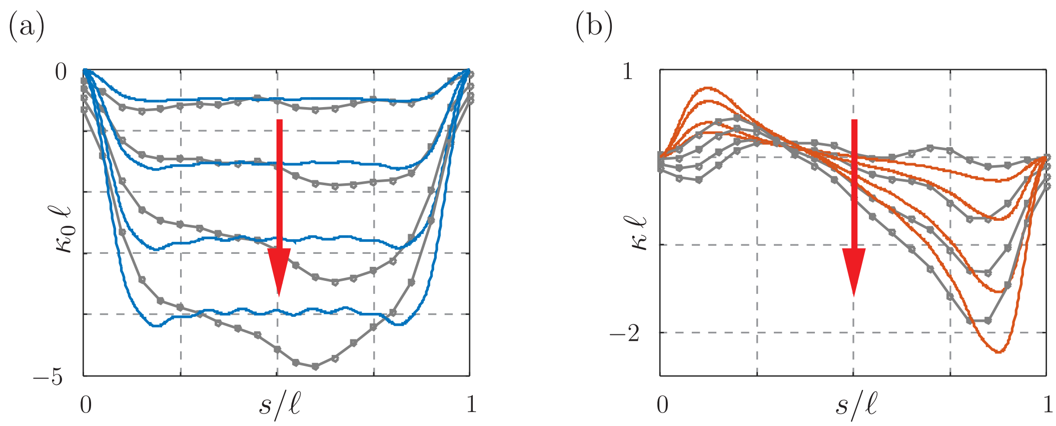

Figure 8: *Curvature of measured and simulated (a) pressurized actuator and (b) additionally loaded actuator. The pressure p in this figure takes the values 5, 17, 31 and 45 kPa and the arrows indicate increasing values. The dotted lines correspond to the measured data from experiments for Test II and Test III. The respective deformed shapes of the centerline were shown earlier in Figure 6.*

A representative set of results for the relation (4) for the bending moment is shown in Figure 2(b) and typically we find that we need five parameters: a pair of flexural stiffnesses $\alpha_{1,2}$, two intercepts $m_{0_{1,2}}$, and the position $s = d$ of the discontinuity. We emphasize that these parameters must be supplemented by the function $\kappa_0\,(s, p)$. Figure 8 shows the intrinsic curvature profile $\kappa_0(s, p)$ and the current curvature profile $\kappa(s, p)$ computed from the experiments and finite element simulations displayed in Figure 6. Observe that the middle section of the soft actuator has an almost constant intrinsic curvature which leads to a circular deformation. By way of contrast, the curvature in Test III changes its sign and has a curvature with a non-zero slope in the middle section.

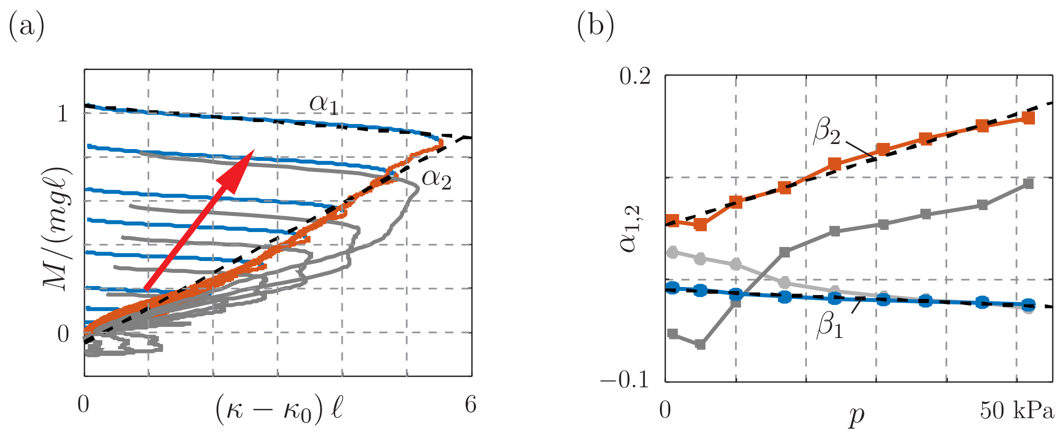

Figure 9: *Measured and simulated (a) dimensionless bending moment $M/(mg\ell)$ as a function of $(\kappa - \kappa_0)\,\ell$ with the flexural rigidity $\alpha_{1,2}$ (slopes of bisected curve) and increasing values of pressure indicated by the arrow, and (b) the flexural rigidity as a linear function of pressure with slope $\beta_{1,2}$ indicated by the dashed lines. The gray lines correspond to the measured data.*

The graphical representation of the relation (4) for the bending moment is displayed in Figure 9(a). This figure shows the non-linear relation of the moment and curvature that we observed in our earlier experimental work that is reported in de Payrebrune and O'Reilly (2016b). For convenience, the bending moment is non-dimensionalized using the length ℓ and weight mg of the unpressurized actuator. Clearly, two distinct sections are visible with distinct flexural rigidities, which we denote by α_1 and α_2, two intercepts which we denote by m_{0_1} and m_{0_2}, and an arc-length parameter d at which the flexural rigidity changes:

$$D(s) = \begin{cases} \alpha_1(s) & s \in [0, d), \\ \alpha_2(s) & s \in (d, \ell]. \end{cases} \tag{8}$$

Values for the rigidities as the pressure is varied are shown in Figure 9(b). For the investigated geometry, d should not exceed the position of the maximum curvature (Figure 8(b)) and this parameter typically takes values ranging between 0.126ℓ and 0.134ℓ.

4. Validation and scalability of the rod model

To validate the parameterization, we compared results from the rod model and those from the finite element model for a given set of end loads. As can be seen from Figure 10(a,b), there is good agreement between the results for both Test II and Test III.

We also note that in addition to the intrinsic curvature and the flexural rigidity, the position d of the discontinuity is an important parameter of the rod model. and is strongly related to the pressure and geometry of the actuator. Complementary investigations of d related to the pressure p and the cavities height H (cf. Figure 11(a)) of the actuator gives a linear approximation within the observed limits of $5 \leq p \leq 40$kPa and $4 \leq H \leq 19$mm. Further information are also provided in our earlier work de Payrebrune and O'Reilly (2016a).

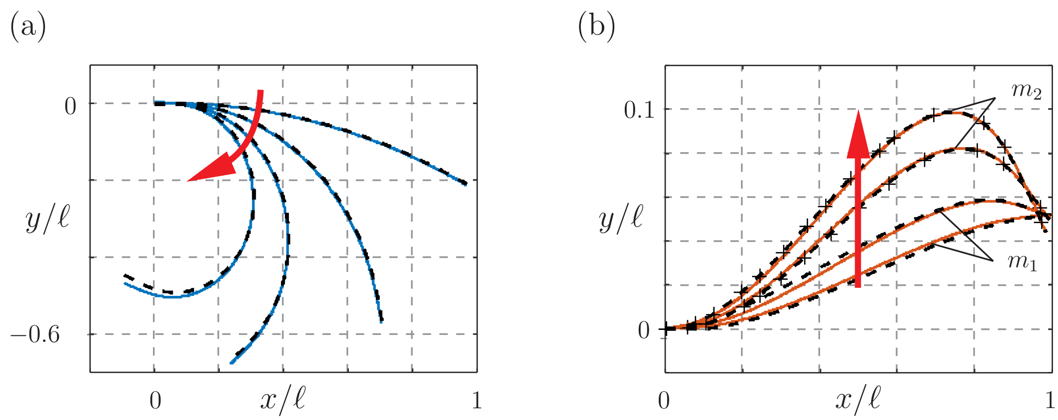

Figure 10: *Deformation obtained by the finite element ((a) blue and (b) red curves) and the rod (black curves) models of (a) a pressurized actuator and of (b) an additionally loaded actuator. The pressure p in this figure takes the values 5, 17, 31 and 45 kPa and the arrows indicate increasing values. The dashed lines illustrate the rod model with the label m_1 indicating $d = 0.1\ell$ and the label m_2 indicating $d = 0.125\ell$.*

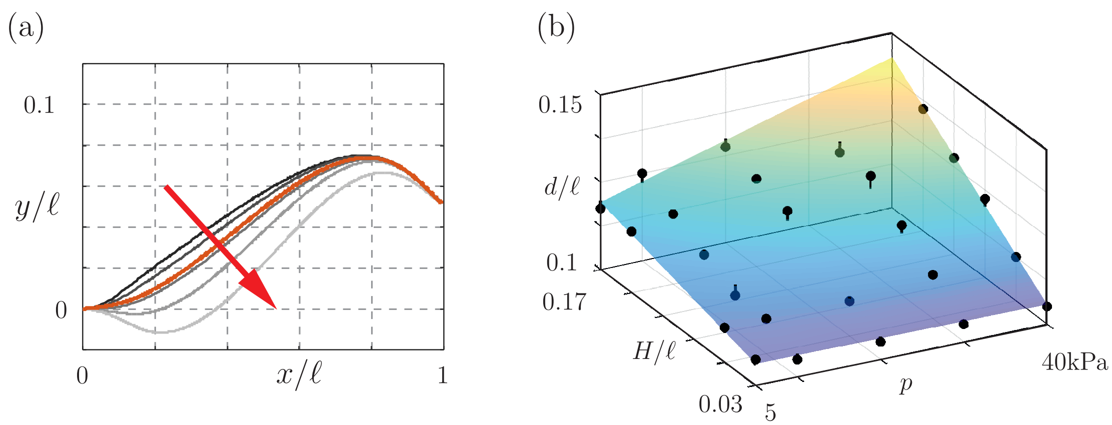

Figure 11: *Deformation obtained by the finite element (red curve) and the rod (grayscale curves) models of a loaded and pressurized actuator with $p = 24$ kPa and varying $d/\ell =$ 0.05, 0.1, 0.125, 0.15, and 0.175 (a), increasing values indicated by the arrows. Linear relation of d/ℓ on pressure p and cavity height H/ℓ with optimal values of d/ℓ displayed as dots (b).*

4.1. Scalability of the Parameters

From Figure 9(b), which illustrates the flexural rigidities $\alpha_{1,2}\,(p)$ from Figure 8(a) as a function of pressure, it is observed that the flexural rigidities are linear functions of p. A related conclusion, which we will document later in Figure 15(a), for the intrinsic curvature $\kappa_0\,(s = \ell/2, p)$ at position $s = \ell/2$ can be inferred from Figure 8(a). These circumstances reduces the number of finite element simulations necessary to parameterize the rod model to three. From the simulation of the pressurized actuator (Test II), we obtain the intrinsic curvature profile. Subsequently, two simulations of the loaded actuator (Test III) are necessary to derive the slopes $\beta_{1,2} = \frac{\alpha_{1,2}(p_2)-\alpha_{1,2}(p_1)}{p_2-p_1}$ of the flexural rigidity $\alpha_{1,2}(s, p)$.

We investigated the dependence of M, $\kappa-\kappa_0$, and $\alpha_{1,2}$ on the actual length ℓ_i of the actuator with respect to the reference length ℓ_0 of the actuator used in our earlier experimental and numerical investigations. Figure 12 displays a linear dependence of the moment and curvature on the change of length $\frac{\ell_i}{\ell_0}$ and we can state the relations

$$\begin{aligned}
\kappa_0(s, p_i, \ell_i) &= \kappa_0(s, p_0, \ell_0) \cdot \frac{p_i}{p_0}\frac{\ell_i}{\ell_0}, \\
\alpha_{1,2}(p_i, \ell_i) &= \Big[\alpha_{1,2}(p_0, \ell_0) + (p_i - p_0)\,\beta_{1,2}(\ell_0)\Big] \left(\frac{\ell_0}{\ell_i}\right)^2,
\end{aligned} \tag{9}$$

with the reference parameters $p = p_0$ and $\ell = \ell_0$. Regarding the limits of $\alpha_{1,2}\,(\cdot, \ell_i)$ as the length of the actuator was varied and $\Delta p = p_i - p_0$ stays fixed, we found that

$$\begin{aligned}
\alpha_{1,2}(\cdot, \ell_i) &= \lim_{\ell_i \to 0} \Big[\alpha_{1,2}(\cdot, \ell_0) + \Delta p_{\text{fix}}\,\beta_{1,2}(\ell_0)\Big] \left(\frac{\ell_0}{\ell_i}\right)^2 = \pm\infty, \\
\alpha_{1,2}(\cdot, \ell_i) &= \lim_{\ell_i \to \infty} \Big[\alpha_{1,2}(\cdot, \ell_0) + \Delta p_{\text{fix}}\,\beta_{1,2}(\ell_0)\Big] \left(\frac{\ell_0}{\ell_i}\right)^2 = \pm 0.
\end{aligned} \tag{10}$$

Here, we have denoted Δp by Δp_{fix} to emphasize that it remains constant during the limiting process. Thus, a soft actuator behaves like a rigid body for $\ell_i \to 0$, and as a string without flexural rigidity as $\ell_i \to \infty$ (cf. Figure 13).

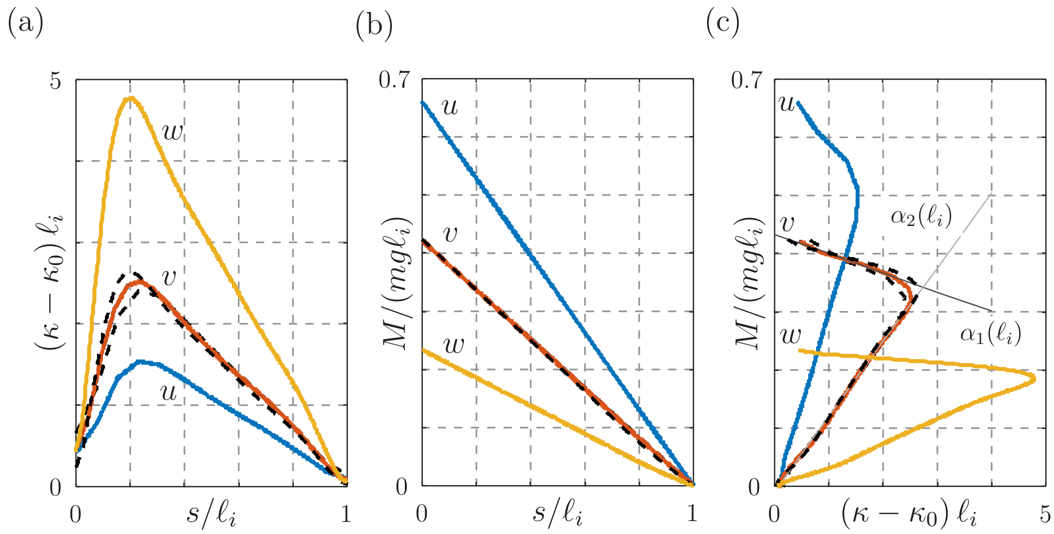

Figure 12: *Influence of the length ℓ_i of the actuator obtained by the finite element model for (a) the difference of current and intrinsic curvature, (b) the moment for an actuator with the boundary condition $y(\ell_i) = 0$, and (c) the moment as a function of $(\kappa - \kappa_0)\,\ell_i$. Values scaled by ℓ/ℓ_0 are indicated by the dashed lines. The labels u, v, and w correspond to the following lengths: u: $\ell_i = 0.64\ell_0$, v: $\ell_i = \ell_0$, and w: $\ell_i = 1.8\ell_0$.*

With the scaling relations $(9)_{1,2}$, the rod model can be easily parameterized and used to evaluate the deforming behavior of a soft actuator for various pressures and lengths. As indicated in Figure 12(c) by the dashed lines, the 5-parameter model remains valid.

4.2. Adaptation to Other Geometries

To validate the parameterization and scalings discussed, we modeled actuators similar to those developed in Suzumori et al. (2007) and Holland

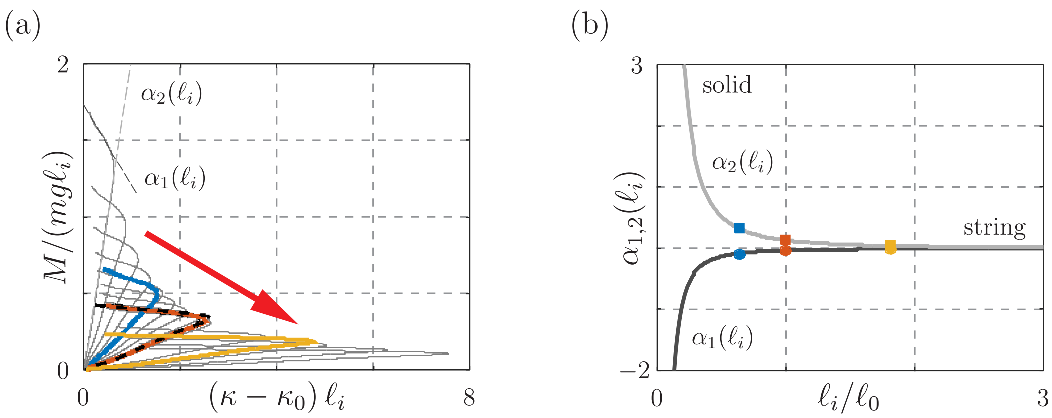

Figure 13: *Development of (a) the moment $M/(mg\ell_i)$ as a function of $(\kappa - \kappa_0)\ell_i$ for various lengths of the actuator and (b) the flexural rigidity $\alpha_{1,2}$ as a function of ℓ_i/ℓ_0. The increasing length of the actuator is indicated by the arrow and the three finite element simulations highlighted by colors from Figure 12.*

et al. (2014). Preliminary analyses of different geometries show that the 5-parameter constitutive relation (shown in Figure 2(b)) is applicable for these designs as well. The linear dependence of the intrinsic curvature and flexural rigidity on the pressurization, however, is strongly related to the actuator's design. For the geometries illustrated in Figure 14, we repeated the finite element simulations to determine the intrinsic curvature profile and flexural rigidities. Figure 15 illustrates the intrinsic curvature $\kappa_0\,(s = \ell/2, p)$ at a specific position $s = \ell/2$ of the actuator and the flexural rigidities $\alpha_{1,2}$ as a function of pressure. While the intrinsic curvature has a linear trend for the entire pressure regime for geometry (a), for the geometries (b), (c) and (d) of Figure 14 the pressure needs to be greater than 20 kPa for such a linear trend to occur.

In the case of the flexural rigidity α_2, this stiffness increases with rising pressure p for geometries with separated cavities (geometries (a) and

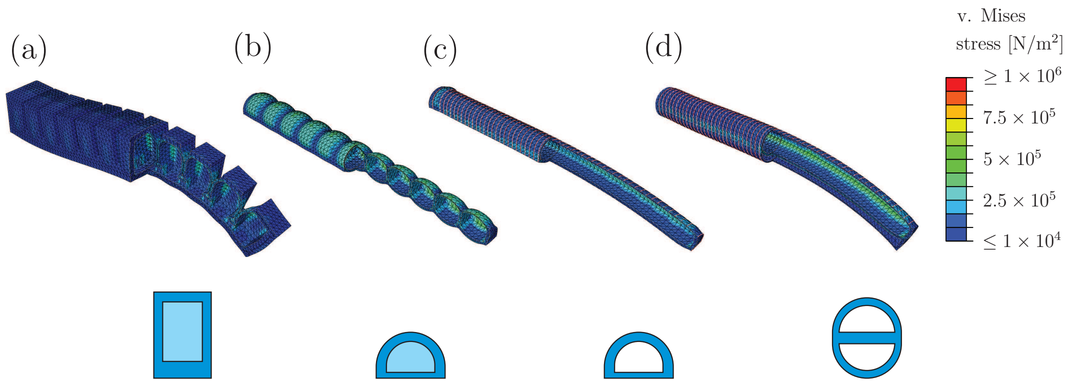

Figure 14: *Deformation of (a) a rectangular actuator with 11 cavities, (b) a semicircular actuator with 11 cavities, (c) a semicircular actuator with one cavity, and (d) a bisected circular actuator. The pressurization is $p = 37$ kPa. One end of the actuator is fixed and the vertical displacement of the other end is prescribed.*

(b)), whereas the rigidity decreases with increasing pressure for geometries with just one cavity along the axis (geometries (c) and (d)) as shown in Figure 15(c). For the case of α_1, this trend is reversed. The non-linear characteristic of rigidity and intrinsic curvature consequently restricts the scaling arguments presented for parameterizing rod models to higher pressure with $p \geq 20$ kPa and makes a closer examination of the geometry necessary. However, the parameter values in the lower pressure regime can be easily obtained by additional finite element simulations.

5. Concluding Remarks

The five-parameter constitutive relation found in de Payrebrune and O'Reilly (2016b) for a specific geometry is also applicable to other soft actuator designs. For instance, we simulated the deformation of the four aforementioned designs using rod and finite element models. The results, shown

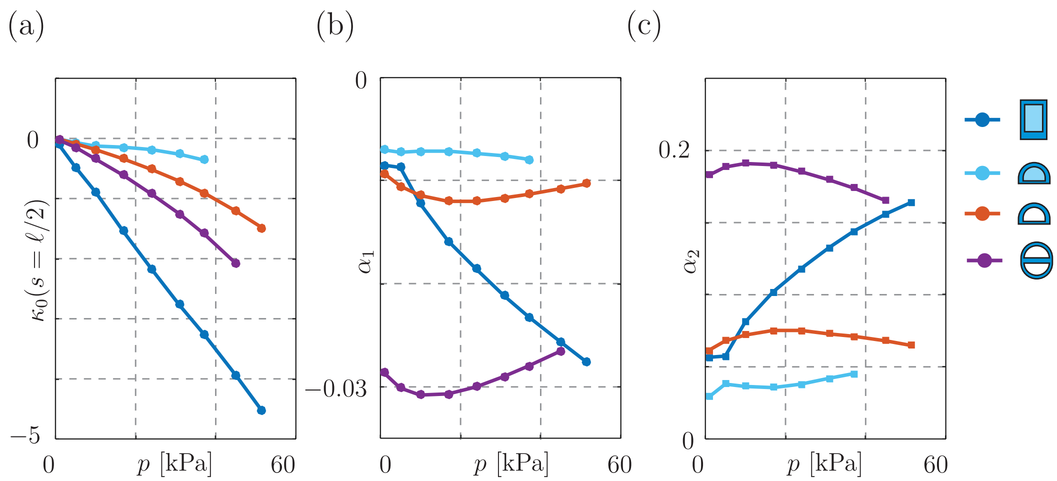

Figure 15: *Pressure dependent (a) change of intrinsic curvature at $s = \ell/2$, (b) change of the flexural rigidity α_1 and (c) of the flexural rigidity α_2 for the actuator geometries shown in Figure 14.*

in Figure 16 demonstrate good agreement between the finite element model, which uses a St. Venant-Kirchhoff constitutive relation, and a rod model which uses a 5-parameter constitutive model. The precise parameters of the constitutive relation can be determined using finite element simulations and, for distinct regimes of pressure, can be found using scaling arguments. The constitutive model can be used in rod-based models for pneumatically actuated limbs in ambulatory soft robots and gripping soft robots and is not restricted to pneunet actuators.

Depending on the geometry of the soft actuator and its deformation during pressurization, the intrinsic curvature and flexural rigidity can be linear functions of the pressure and the length of the actuator. We found that actuators with a single cavity tend to have a non-linear dependence on pressure in the low pressure regime. Further, the dependence on the parameter d is strongly related to supporting effects of the structure of the soft actuator. In particular, for the pneu-net actuator, the chamber walls tended to contact each other during some modes of deformation, which led to a difference in stiffness compared to those segments where no self contact of the chambers occurred.

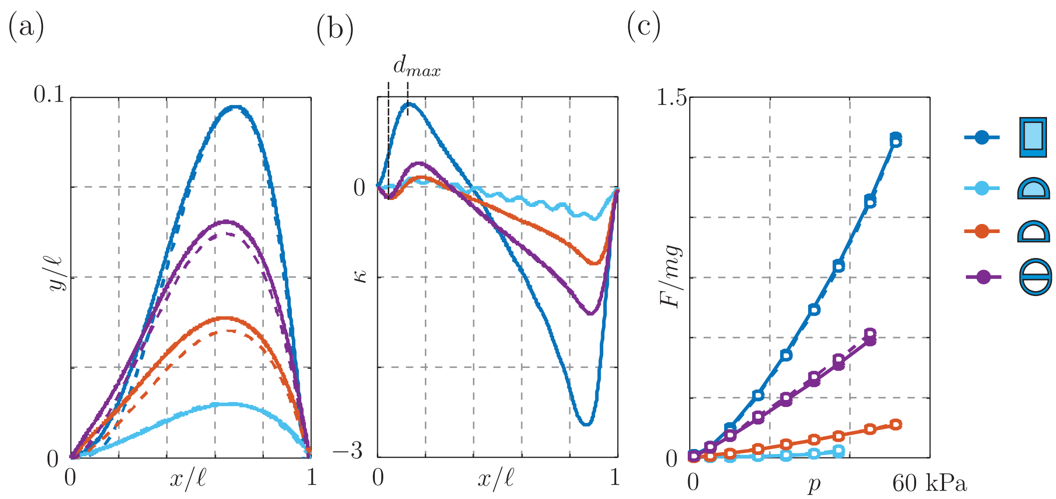

Figure 16: *Calculated deformation using the finite element model (solid lines) and rod model (dashed lines) for* $p = 37$ *kPa (a), final curvature for* $p = 37$ *kPa (b), and forces at the end position in vertical direction (c), with respect to the pressurization for the four geometries shown in Figure 14. The length of section* $\alpha_1(s)$ *with* $s \in [0, d)$ *is* $d = 0.14\ell$ *for the soft actuator shown in Figure 3 and* $d = 0.048\ell$ *for the additionally investigated geometries.*

6. Conflicts of Interest

None of the authors have a conflict of interest.

7. Acknowledgements

We take this opportunity to thank the Institute for Machine Elements, Design and Manufacturing (IMKF) at the Technische Universität Bergakademie Freiberg where we conducted the tensile tests. During the course of this research, Dr. de Payrebrune was supported by a grant from the German Research Foundation (DFG) PA2553/1-1. The work of O'Reilly was partially supported by grant number W911NF-16-1-0242 from the U.S. Army Research Office under the program manager Dr. Sam Stanton. We also thank Abdulrahman Jbaily for his helpful comments on an earlier draft and an anonymous reviewer for their thoughtful and constructive criticisms that helped improve the paper.

References

Aissiou, M., Périé, D., Gervais, J., Trochu, F., 2013. Development of a progressive dual Kriging technique for 2D and 3D multi-parametric MRI data interpolation. Computer Methods in Biomechanics and Biomedical Engineering: Imaging & Visualization 1 (2), 69–78.
URL http://dx.doi.org/10.1080/21681163.2013.765712

Calisti, M., Giorelli, M., Levy, G., Mazzolai, B., Hochner, B., Laschi, C., Dario, P., 2011. An octopus-bioinspired solution to movement and manipulation for soft robots. Bioinspiration & Biomimetics 6 (3), 036002.
URL http://stacks.iop.org/1748-3190/6/i=3/a=036002

de Payrebrune, K. M., O'Reilly, O. M., 2016a. An experimentally validated

rod model for soft continuum robots. PAMM 16 (1), 317–318.
URL http://dx.doi.org/10.1002/pamm.201610147

de Payrebrune, K. M., O'Reilly, O. M., 2016b. On constitutive relations for a rod-based model of a pneu-net bending actuator. Extreme Mechanics Letters 8, 38–46.
URL http://dx.doi.org/10.1016/j.eml.2016.02.007

Gravagne, I., Rahn, C. D., Walker, I. D., 2003. Large deflection dynamics and control for planar continuum robots. Mechatronics, IEEE/ASME Transactions on 8 (2), 299–307.
URL http://ieeexplore.ieee.org/stamp/stamp.jsp?tp=&arnumber=1206487&isnumber=27144

Holland, D. P., Park, E. J., Polygerinos, P., Bennett, G. J., Walsh, C. J., 2014. The Soft Robotics Toolkit: Shared resources for research and design. Soft Robotics 1 (3), 224–230.
URL http://dx.doi.org/10.1089/soro.2014.0010

Ilievski, F., Mazzeo, A. D., Shepherd, R., Chen, X., Whitesides, G. M., 2011. Soft robotics for chemists. Angewandte Chemie 123, 1930–1935.
URL http://dx.doi.org/10.1002/ange.201006464/full

Kim, S., Laschi, C., Trimmer, B., 2013. Soft robotics: a bioinspired evolution in robotics. Trends in Biotechnology 31 (5), 287 – 294.
URL http://dx.doi.org/10.1016/j.tibtech.2013.03.002

Majidi, C., 2013. Soft robotics: A perspective - current trends and prospects

for the future. Soft Robotics 1, 5–11.
URL http://dx.doi.org/10.1089/soro.2013.000

Majidi, C., O'Reilly, O., Williams, J., 2012. On the stability of a rod adhering to a rigid surface: Shear-induced stable adhesion and the instability of peeling. Journal of the Mechanics and Physics of Solids 60 (5), 827 – 843.
URL http://www.sciencedirect.com/science/article/pii/S0022509612000233

Majidi, C., Shepherd, R. F., Kramer, R. K., Whitesides, G. M., Wood, R. J., 2013. Influence of surface traction on soft robot undulation. The International Journal of Robotics Research 32 (13), 1577–1584.
URL http://dx.doi.org/10.1177/0278364913498432

Marchese, A. D., Onal, C. D., Rus, D., 2014. Autonomous soft robotic fish capable of escape maneuvers using fluidic elastomer actuators. Soft Robotics 1 (1), 75–87.
URL http://dx.doi.org/10.1089/soro.2013.0009

Martinez, R. V., Branch, J. L., Fish, C. R., Jin, L., Shepherd, R. F., Nunes, R., Suo, Z., Whitesides, G. M., 2013. Robotic tentacles with three-dimensional mobility based on flexible elastomers. Advanced Materials 25 (2), 205–212.
URL http://dx.doi.org/10.1002/adma.201203002

Pfeifer, R., Lungarella, M., Iida, F., 2012. The challenges ahead for bio-inspired 'soft' robotics. Communications of the Association for Computing Machinery ACM 55 (11), 76–87.

URL http://cacm.acm.org/magazines/2012/11/156584-the-challenges-ahead-for-bio-inspired-soft-robotics/fulltext

Plaut, R. H., 2015. Mathematical model of inchworm locomotion. International Journal of Non-Linear Mechanics 76, 56–63.
URL http://www.sciencedirect.com/science/article/pii/S0020746215001080

Polygerinos, P., Lyne, S., Wang, Z., Nicolini, L. F., Mosadegh, B., Whitesides, G. M., Walsh, C. J., 2013. Towards a soft pneumatic glove for hand rehabilitation. In: Intelligent Robots and Systems (IROS), 2013 IEEE/RSJ International Conference on. IEEE, pp. 1512–1517.
URL http://ieeexplore.ieee.org/stamp/stamp.jsp?tp=&arnumber=6696549&isnumber=6696319

Renda, F., Cianchetti, M., Giorelli, M., Arienti, A., Laschi, C., 2012. A 3D steady-state model of a tendon-driven continuum soft manipulator inspired by the octopus arm. Bioinspiration & Biomimetics 7 (2), 025006.
URL http://iopscience.iop.org/article/10.1088/1748-3182/7/2/025006/meta;jsessionid=E54544601B368BA8F51F635040741F17.c4.iopscience.cld.iop.org

Santillan, S., Virgin, L., Plaut, R., 2006. Post-buckling and vibration of heavy beam on horizontal or inclined rigid foundation. Journal of Applied Mechanics 73 (4), 664–671.
URL http://dx.doi.org/10.1115/1.2165237

Shepherd, R., Ilievski, F., Choi, W., Morin, S., Stokes, A., Mazzeo, A., Chen, X., Wang, M., Whitesides, G., 2011. Multigait soft robot. Proceedings of the National Academy of Sciences.
URL http://dx.doi.org/10.1073/pnas.1116564108

Soft Robotics Toolkit, 2017. Soft robotics toolkit. http://softroboticstoolkit.com/book/pneunets-modeling, accessed: 2017-02-07.

Stokes, A. A., Shepherd, R. F., Morin, S. A., Ilievski, F., Whitesides, G. M., 2014. A hybrid combining hard and soft robots. Soft Robotics 1 (1), 70–74.
URL http://dx.doi.org/10.1089/soro.2013.0002

Suzumori, K., 1996. Elastic materials producing compliant robots. Robotics and Autonomous Systems 18 (1), 135–140.
URL http://dx.doi.org/10.1016/0921-8890(95)00078-X

Suzumori, K., Endo, S., Kanda, T., Kato, N., Suzuki, H., 2007. A bending pneumatic rubber actuator realizing soft-bodied manta swimming robot. In: Robotics and Automation, 2007 IEEE International Conference on. IEEE, pp. 4975–4980.
URL http://dx.doi.org/10.1109/ROBOT.2007.364246

Suzumori, K., Maeda, T., Wantabe, H., Hisada, T., 1997. Fiberless flexible microactuator designed by finite-element method. Mechatronics, IEEE/ASME Transactions on 2 (4), 281–286.
URL http://ieeexplore.ieee.org/stamp/stamp.jsp?tp=&arnumber=653052&isnumber=14234

Tolley, M. T., Shepherd, R. F., Mosadegh, B., Galloway, K. C., Wehner, M., Karpelson, M., Wood, R. J., Whitesides, G. M., 2014. A resilient, untethered soft robot. Soft Robotics 1 (3), 213–223.
URL http://dx.doi.org/10.1089/soro.2014.0008

Webster, R. J., Jones, B. A., 2010. Design and kinematic modeling of constant curvature continuum robots: A review. The International Journal of Robotics Research.
URL http://ijr.sagepub.com/content/early/2010/06/09/0278364910368147.abstract

Yang, D., Mosadegh, B., Ainla, A., Lee, B., Khashai, F., Suo, Z., Bertoldi, K., Whitesides, G. M., 2015. Buckling of elastomeric beams enables actuation of soft machines. Advanced Materials 27 (41), 6323–6327.
URL http://dx.doi.org/10.1002/adma.201503188

Zhou, X., Majidi, C., O'Reilly, O. M., 2015. Flexing into motion: A locomotion mechanism for soft robots. International Journal of Non-Linear Mechanics 74, 7–17.
URL http://dx.doi.org/10.1016/j.ijnonlinmec.2015.03.001